

# Crystalline phases at finite winding densities in a quantum link ladder

Paolo Stornati,<sup>1,\*</sup> Philipp Krah,<sup>2</sup> Karl Jansen,<sup>3</sup> and Debasish Banerjee<sup>4,5</sup>

<sup>1</sup>*ICFO-Institut de Ciències Fotoniques, The Barcelona Institute of Science and Technology, Av. Carl Friedrich Gauss 3, 08860 Castelldefels (Barcelona), Spain*

<sup>2</sup>*TU Berlin, Institute of Mathematics, Straße des 17. Juni 136, 10623 Berlin, Germany*

<sup>3</sup>*Deutsches Elektronen-Synchrotron DESY, Platanenallee 6, 15738 Zeuthen, Germany*

<sup>4</sup>*Theory Division, Saha Institute of Nuclear Physics, 1/AF Bidhan Nagar, Kolkata 700064, India*

<sup>5</sup>*Homi Bhabha National Institute, Training School Complex, Anushaktinagar, Mumbai 400094, India*

Condensed matter physics of gauge theories coupled to fermions can exhibit a rich phase structure, but are nevertheless very difficult to study in Monte Carlo simulations when they are afflicted by a sign problem. As an alternate approach, we use tensor network methods to explore the finite density physics of Abelian gauge theories without dynamical matter. As a concrete example, we consider the  $U(1)$  gauge invariant quantum link ladder with spin- $\frac{1}{2}$  gauge fields in an external electric field which cause the winding electric fluxes to condense in the ground state. We demonstrate how the electric flux tubes arrange themselves in the bulk giving rise to crystalline patterns, whose period can be controlled by tuning the external field. We propose observables to detect the transitions in ground state properties not only in numerical experiments, but also in future cold-atom realizations. A systematic procedure for reaching the thermodynamic limit, as well as extending the studies from ladders to extended geometries is outlined.

*Introduction.*— Finite chemical potentials are expected to give rise to novel phases and correlations otherwise absent in the ground state of quantum field theories or quantum many-body systems. Two physically relevant examples are Quantum Chromodynamics (QCD) and the Hubbard model. Markov Chain Monte Carlo (MCMC) methods to solve QCD regulated on the lattice can explain properties of hadrons, such as their masses, binding energies, and scattering cross-sections. At finite baryon densities,  $\mu_B$ , relevant for e.g., the description of the interior of neutron stars or the very early universe, the MCMC methods suffer from the infamous sign problem. The Hubbard model, on the other hand, is a pedagogical system to describe a variety of phases of strongly correlated electrons. At finite doping, it is expected to host high-temperature superconducting phases and provide a model for many physically interesting materials. Once again, the regime of non-zero doping is difficult to investigate numerically using Monte Carlo methods due to the sign problem.

Finite density physics of scalar and fermionic theories in various space-time dimensions have been extensively investigated [1–7]. We extend such studies which dealt with point particles to pure gauge theories without dynamical matter fields containing loop operators. The simplest scenario is an  $U(1)$  Abelian lattice gauge theory in a finite volume and in 2+1 dimensions, where gauge-invariant winding electric flux strings can be excited by coupling a chemical potential to each of the global  $U(1)$  centre-symmetry generators. Each sector is labelled by a set of integers  $(\mathbb{Z}_1, \mathbb{Z}_2)$ , indicating the number of windings in a specified spatial direction. Moreover, these sectors are topological in nature, and states in a given winding number sector cannot be smoothly deformed to another sector. Further, the electric flux tubes are non-

local extended excitations, unlike the point-like bosonic or fermionic particles, and their properties at finite densities could in principle be considerably different.

Flux tubes have been played a prominent role in the description of various physical phenomena. Nielsen and Olesen [8] introduced the field theory of a vortex-line model, also identified with dual strings. These are flux tubes, similar to the ones that occur in the theory of type-II superconductors, and are responsible for most of the low-energy physics in the strong coupling limit. Classical and semi-classical analysis involving electric fluxes interacting with a gas of monopoles, giving rise to confinement have been discussed in [9, 10]. Non-abelian generalizations of such operators, called disorder operators, were introduced by 't Hooft to analyse the phases of non-Abelian gauge theories [11].

We consider the condensed matter physics of these flux tubes in 2+1-dimensional  $U(1)$  gauge theory. Previous studies have used the path integral formulation by either exploiting the dual representation of Abelian lattice gauge theories [12, 13], or by using the multilevel algorithm [14] and explored properties such as the profile of the electric flux lines connecting static charges, or the variation of the potential between two charges with increasing the representation of the charges. Among other things, this provides valuable insights about the attractive or repulsive nature of the flux tubes.

In this article, we use the Hamiltonian formulation of a  $U(1)$  quantum link ladder (QLL) [15]. This theory is known to have novel crystalline confined phases which carry fractional electric flux excitations [16], possess anomalously localized excited states [17], and are the building blocks of spin-ice compounds [18, 19]. While it is known how to simulate the theory with an improved cluster algorithm at zero and finite temperature [20], this

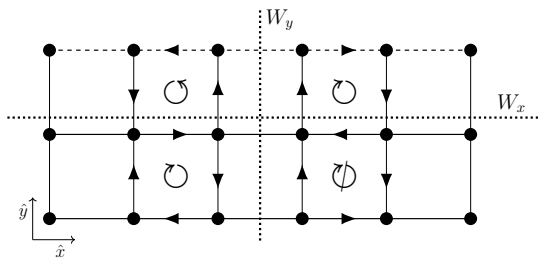


**FIG. 1:** Ladder geometry of the lattice. The periodicity in  $\hat{y}$  is indicated by the dashed lines. Two flippable plaquettes ( $\odot$ ,  $\circ$ ) and a non flippable plaquette ( $\Phi$ ) are also shown. The dotted lines indicate the links which need to be summed to obtain the  $x$ - and  $y$ -windings.

method has not been extended to deal with the scenario at finite winding chemical potential. Instead, we use tensor network methods (see for review [21]) to perform an ab-initio study of the system at finite winding density. Thanks to the rapid development of quantum simulators, the key elements for realizing this microscopic model on digital and analogue quantum computers are already available [22–24]. The finite density physics investigated in the article is ideal to be observed in a quantum computing setup. The open boundaries and gauge invariance realized with quantum spin operators are very natural for quantum simulators.

*The  $U(1)$  quantum link ladder.*— To illustrate our ideas, we consider the setup of the  $U(1)$  QLL with the gauge fields represented by quantum spins in the spin- $\frac{1}{2}$  representation on a rectangular lattice  $L_x \times L_y$ , with  $L_y = 2$  and  $L_x = 6, \dots, 64$ , illustrated in Figure 1. Each link degree of freedom has a two-dimensional Hilbert space, and the gauge field operator raises (or lowers) the electric flux basis state:  $U_{r,\hat{i}} = S_{r,\hat{i}}^+$ ,  $U_{r,\hat{i}}^\dagger = S_{r,\hat{i}}^-$ ,  $E_{r,\hat{i}} = S_{r,\hat{i}}^z$ . The Hamiltonian consists of two types of plaquette operators:

$$\mathcal{H}_\square = -J \sum_{\square} (U_\square + U_\square^\dagger) + \lambda \sum_{\square} (U_\square + U_\square^\dagger)^2, \quad (1)$$

where  $U_\square = U_{r,\hat{i}} U_{r+\hat{i},\hat{j}} U_{r+\hat{j},\hat{j}} U_{r,\hat{j}}^\dagger$ . One could have added the square of the electric field energy  $\sum_{r,\hat{i}} E_{r,\hat{i}}^2$ , but for the spin- $\frac{1}{2}$  representation, this is a trivial constant and can be neglected. As shown in Figure 1, the first operator flips any flippable plaquette, while the second operator counts the total number of flippable plaquettes. Only two of the 16 states on a plaquette are non-trivially acted upon by the plaquette operators. The reduction in the number of physical states is due to a local  $U(1)$  symmetry, generated by the Gauss law

$$G_r = \sum_{\hat{i}=\hat{x},\hat{y}} (E_{r-\hat{i},\hat{i}} - E_{r,\hat{i}}) = \sum_{\hat{i}=\hat{x},\hat{y}} (S_{r-\hat{i},\hat{i}}^z - S_{r,\hat{i}}^z). \quad (2)$$

Physical states satisfy  $G_r |\psi\rangle = 0$ , which implies the absence of any charge on the lattice. In addition, the model

has several global symmetries: the lattice translation symmetry (by one lattice spacing), the reflection and the rotation symmetry. In addition, there is the  $Z_2$  charge conjugation symmetry:  $U \rightarrow U^\dagger$ ,  $E \rightarrow -E$ . However, the main object of our interest are the  $U(1)^2$  global winding number symmetries, generated by the operators:

$$W_x = \frac{1}{2L_y} \sum_r S_{r,\hat{y}}^z \quad \text{and} \quad W_y = \frac{1}{2L_x} \sum_r S_{r,\hat{x}}^z. \quad (3)$$

where the sum over  $r$  runs over all lattice sites. These operators commute with the Hamiltonian and thus classify the eigenstates in terms of the number of times the flux loops wind the system either along the  $x$ - or the  $y$ -direction. Therefore, it is natural to couple chemical potentials with strengths  $\mu_x, \mu_y$  to the Hamiltonian and extend the full Hamiltonian as:  $\mathcal{H} = \mathcal{H}_\square - \mu_x W_x - \mu_y W_y$ .

The windings  $W_{x,y}$  are good quantum numbers for periodic boundary conditions. However, for using open boundary conditions (as we impose in the longer directions, since we use matrix product states (MPS) in our calculations), one can show that an external field  $(h_x, h_y)$  that couples to the  $x$ -links and  $y$ -links respectively serves the same purpose, keeping  $W_{x,y}$  to be good quantum numbers. With the external field, there is a non-trivial contribution from the kinetic energy term:  $\sum_{r,\hat{x}} (E_{r,\hat{x}} - h_x)^2 + \sum_{r,\hat{y}} (E_{r,\hat{y}} - h_y)^2 = -h_x \sum_{r,\hat{x}} E_{r,\hat{x}} - h_y \sum_{r,\hat{y}} E_{r,\hat{y}} + \text{const} = -2h_x W_y - 2h_y W_x + \text{const}$ , which is equivalent to coupling the system with  $\mu_{x,y}$ . We will use the latter notation for the rest of the article.

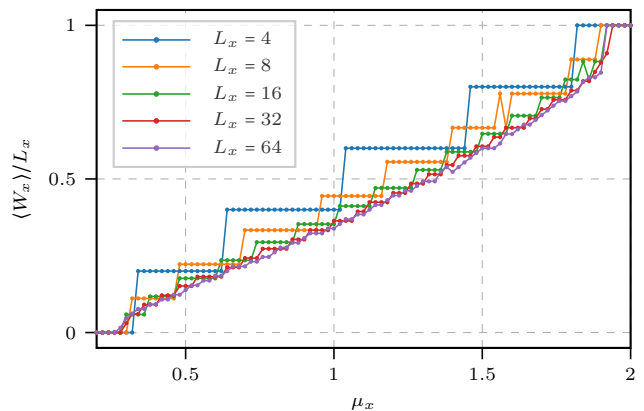


**FIG. 2:** Staircase structure of the winding numbers  $\langle W_x \rangle$  with increasing  $\mu$ . The plateaus correspond to ground states where the winding flux remains fixed as  $\mu$  is varied. In the thermodynamic limit, the curve becomes continuous. For large  $\mu$ , the curve saturates just as for fermion (or hard-core bosons).

*Numerical methods.*— We begin by noting that the model considered here a rich ground state phase diagram [16] and realizes novel crystalline confined phases. The physics of excited states have revealed the existence of quantum scar states, and atypical real-time dynamics

[17]. While the former used an efficient cluster Monte-Carlo algorithm, the latter used large scale exact diagonalization (ED). In this work, we aim to go for system sizes beyond the reach of ED, but efficient algorithms at finite  $\mu$  are non-trivial to construct. While the existing cluster algorithms can update all sectors at finite temperatures, it is unclear on how to extend this algorithm for finite  $\mu$ . Therefore, we use density matrix renormalization group (DMRG) on MPS states to simulate the ground state phases with increasing values of  $\mu = \sqrt{\mu_x^2 + \mu_y^2}$ . The  $\mu_y = 0$  is kept throughout the calculations to ensure that there is no condensation of strings in the  $y$ -direction.

*Condensation of strings.*— The effect of increasing  $\mu_x$  on various system sizes is shown in Figure 2. The more familiar examples of condensation phenomena are known from bosons and fermions, which are point particles. We notice that with flux strings, too, one has the "silver blaze" problem, in which the ground state is unaffected by the chemical potential until a threshold value  $\mu_c(L_x)$  is reached, after which the vacuum becomes unstable to the creation of net flux strings periodically winding around  $L_y$ . On the smaller lattices, one can clearly observe the step-like structure that results, with each step indicating the number of winding strings that have condensed in the vacuum. Plotted in terms of the winding density, we notice the smooth approach to the thermodynamic limit in the data for lattices when reaching  $L_x = 64$  (see Figure 2). Note in particular that both the threshold chemical potential,  $\mu_c(L_x)$ , at which condensation phenomena starts and the saturation chemical potential  $\mu_s(L_x)$  have well-defined thermodynamic limits. In Figure 3 we show the behaviour of  $\mu_c(L_x)$  with increasing volume. It is interesting to note that the finite volume dependence is very well described with the same formula that governs the dependence of a massive particle in finite volume [25]. We note that the step behaviour of magnetization with an external magnetic field at zero temperature is well known for frustrated spin systems [26]. Recently, a similar behaviour has been reported for the ladder Rydberg systems [27].

While we have demonstrated the thermodynamic limit for  $L_y = 2$  ladders, more work is essential to extend the results to other geometries. In particular, the 2-d system can be thought of as a sequence of ladders with increasing  $L_y$  at each step. At each fixed  $L_y$ , we can first take the  $L_x \rightarrow \infty$  limit. Thus, strings that are in general non-local in  $L_y$  can condense in an infinitely wide ladder. For a confining theory, increasing  $L_y \rightarrow \infty$  is expected to yield  $\mu_c(L_x \rightarrow \infty, L_y)$  that increases linearly with  $L_y$ . We postpone the demonstration of the thermodynamic limit of larger ladders in a future study, and turn to understanding the nature of the phases that are realized in the ground states at finite density.

*Crystalline structures.*— As we demonstrate now, once the winding strings start condensing in the ground state, they modulate existing crystalline properties. At

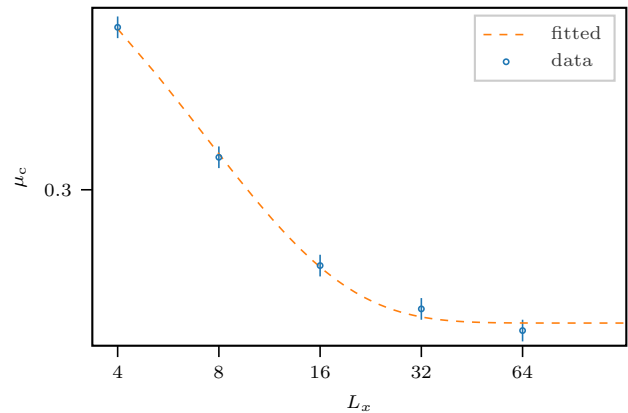


**FIG. 3:** Finite size dependence of  $\mu_c(L_x) = a \exp(-bL_x) + \mu_c^\infty$  on  $L_x$ . From the fit we determine:  $\mu_c^\infty = 0.269$ . The error bars are the magnitude of the finite step  $\Delta_{\mu_x} = 0.0025$  taken to identify the phase transition point.

$\mu_x = 0$  and  $\lambda = -1$ , the ground state breaks both translation invariance and charge conjugation spontaneously [16]. The novel feature at finite  $\mu_x$  is the repulsion of condensed strings in the  $x$ -direction and their subsequent arrangement in periodic intervals. This necessarily modulates the pattern of electric fields,  $E_{T,\hat{i}}$ , from the zero density case.

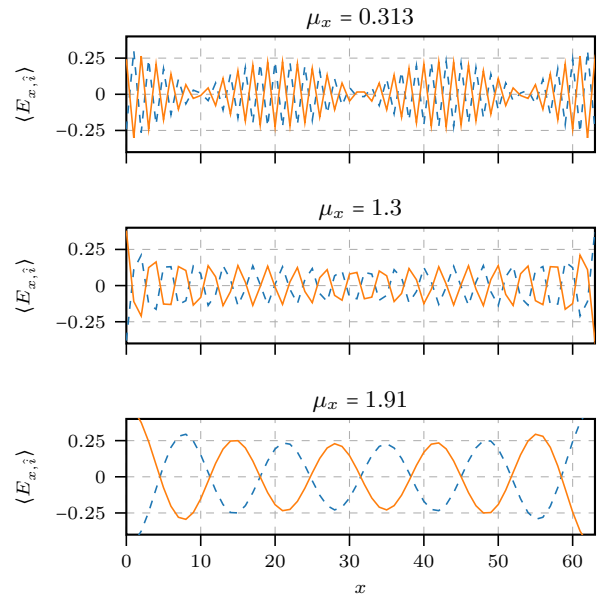


**FIG. 4:** Vertical electric field,  $\langle E_{x,\hat{i}} \rangle$ , for the  $L_x = 64$  lattice for three different regimes of winding density. The dashed lines correspond to the upper rung and solid lines to the electric field on the lower rung of the ladder

In Figure 4, we show the spatial distribution of the fluxes in the  $y$ -direction,  $E_{x,\hat{i}}$ , at three different  $\mu_x$  values for the largest lattice  $L_x = 64$ , representative of three distinct regimes. We call these three different winding regimes: dilute gas regime, half filled and close to satu-

ration regime.

The first regime occurs when the system has just started to condense isolated strings, and the system can be treated as a dilute gas of strings. The top panel of Figure 4 at  $\mu_x = 0.313$  illustrates this case. The three regions where the  $\langle E_{x,\hat{i}} \rangle \approx 0$  marks the location of the winding strings wrapping along the  $y$ -direction. We infer that the preference of the strings to stay as far away from each other as possible is indicative of their repulsive interaction. Moreover, in between the location of the fluxes, the  $\langle E_{x,\hat{i}} \rangle$  displays a regular oscillatory pattern, as also expected for  $\mu_x = 0$ . This arrangement of the fluxes maximizes the total number of flippable plaquettes, as preferred by the  $\lambda = -1$  term in the Hamiltonian.

On increasing the filling fraction of the winding density, we notice that the long-wavelength modulations of the electric flux disappear. As shown in the representative middle panel, for  $\mu_x = 1.3$ , the long-range modulations of  $\langle E_{x,\hat{i}} \rangle$  disappear. The short range oscillations of the horizontal fluxes are still present with twice the period than the previous case: the dashed and the solid lines take their maximum positive and negative values ( $\approx \pm 0.25$ ) 16 times. This regime corresponds to the half-filling of winding strings, now distributed evenly through the system, removing traces of previous spatial modulations. Making the system denser causes one to approach to the saturation regime, where the electric fields further rearrange to produce a smooth coherent oscillation. The bottom panel in Figure 4, for  $\mu_x = 1.91$  shows the coherent oscillations for  $L_x = 64$  in this regime, spread over 12-15 lattice spacing.

We can also understand the physical properties from the sum of the electric fields on the vertical links,  $E_{y,\hat{j}}$ , which provides the analog of the "particle number density". Following our previous discussions, we also expect these profiles to show modulations, which are plotted in Figure 5a for our biggest lattice  $L_x = 64$ . Three distinct regimes are also visible in this plot. The set of blue curves represents the regime where the system has just started to condense isolated strings. It is clear that as  $\mu_x$  is slowly increased, the winding strings condense in such a way as to maintain maximal separation from each other and the highly polarized boundaries. The first such string excitation sits in the middle of the lattice, as shown by the maximum in the density profile. The case with three peaks in  $E_{x,\hat{j}}$  (at  $x = 10a, 30a, 50a$ ) correspond to the profile of  $E_{x,\hat{i}}$  at  $\mu_x = 0.313$  shown in Figure 4. The presence of the fluxes (wrapping vertically) makes the plaquettes non-flippable, which is exactly the locations where the horizontal fields are minimum and the vertical fields maximum, demonstrating that the strings affect all the local properties.

On increasing  $\mu_x$ , the  $E_{x,\hat{j}}$  loses the modulations that identify individual fluxes, and a smooth distribution, modulated more at the boundaries than in the bulk are visible. Closer to the saturation region upon further in-

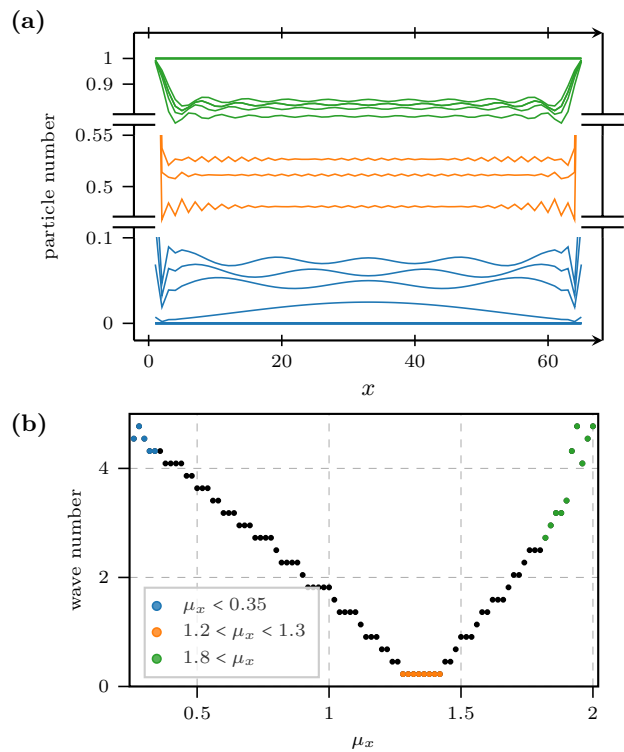


**FIG. 5:** Winding number regimes of the quantum link ladder. (a) The winding number distribution as a function of the distance to one boundary for the three different regimes. (b) The wave number as a function of the chemical potential for the states where the particle number is non-zero or non-saturated. The three different winding regimes are highlighted with colored markers/lines: dilute gas regime ( $\bullet$ ), half filled ( $\circ$ ) and close to saturation regime ( $\circ$ ).

creasing of  $\mu_x$ , again longer ranged smooth modulations of the "particle density" appear, which now stretch over several lattice spacing. Interestingly, this length scale seems to be dynamically generated in this regime and rather sensitive to the external  $\mu_x$ . The wave number of the oscillations can thus be controlled by tuning the  $\mu_x$ .

Figure 5b shows the wave number of the oscillations as a function of  $\mu_x$ , obtained by identifying the dominant wave-number that contributes in the Fourier transform of the vertical electric flux profiles,  $E_{x,\hat{j}}$ . The information in this observable is thus the same as in the structure factor up to a global factor, which is given as a Fourier transform of the electric flux correlation function at a particular momentum  $k$  (the wave number is  $k/2\pi$  in our context). Even in this plot, the aforementioned three regimes in  $\mu_x$  are clearly visible. The first non-trivial excitations for small  $\mu_x$ , present long range oscillations whose wave numbers keep decreasing until they saturate to a small value. This is the regime where the system is approximately half-filled, and for the  $L_x = 64$  spans from  $\mu_x = 1.2, \dots, 1.3$ . In this region, the translational invariance is approximately recovered. When the chemi-

cal potential is increased, the oscillations rise again with a much faster rate, as already apparent from the earlier observables.

*Conclusions and Outlook.*— In this Letter, we have explored the phenomenon of string condensation in an  $U(1)$  Abelian lattice gauge theory realized as a spin-1/2 QLM. We have demonstrated that our ladder system possesses a smooth thermodynamic limit for a fixed  $L_y$ . The system starts to condense strings with the increase in  $\mu_x$ , and the system exhibits at least three different regimes before saturation is reached. Through the profiles of the horizontal and vertical electric fluxes, we have shown that the winding strings arrange themselves in patterns which behave distinctly in each of the three regimes. In the dilute regime, isolated string excitations can be identified, while the half-filled regime is marked by an approximate restoration of translation invariance. In the dense region, there is a dynamically generated length scale which changes rapidly with  $\mu_x$  before the system saturates. Our observables are perfectly suited to be measured in cold atom experiments of lattice gauge theory models [28–33].

There are several directions in which the analysis can be extended. The most obvious is to repeat the calculation for larger ladders and study the different regimes that manifest themselves. Other observables, such as the central charge, and finite size scaling of correlation functions could be useful in attempting to understand if there is a phase transition between the different regimes. The nature of the origin of the length scale in the dense region is also an open question, which might be understood better from an effective field theory approach. Another obvious question is if similar phenomena can also be observed in QLMs in the spin-1 representation, which are very similar to the lattice gauge theory formulation by Wilson.

*Acknowledgements.*— We would like to thank Luca Barbiero, Marcello Dalmonte, Adam Nahum, Arnab Sen, and Uwe-Jens Wiese for helpful discussions.

PS acknowledges support from: ERC AdG NO-QIA; Ministerio de Ciencia y Innovation Agencia Estatal de Investigaciones (PGC2018-097027-B-I00/10.13039/501100011033, CEX2019-000910-S/10.13039/501100011033, Plan National FIDEUA PID2019-106901GB-I00, FPI, QUANTERA MAQS PCI2019-111828-2, QUANTERA DYNAMITE PCI2022-132919, Proyectos de I+D+I “Retos Colaboración” QUSPIN RTC2019-007196-7); European Union NextGenerationEU (PRTR); Fundació Cellex; Fundació Mir-Puig; Generalitat de Catalunya (European Social Fund FEDER and CERCA program (AGAUR Grant No. 2017 SGR 134, QuantumCAT U16-011424, co-funded by ERDF Operational Program of Catalonia 2014-2020); Barcelona Supercomputing Center MareNostrum (FI-2022-1-0042); EU Horizon 2020 FET-OPEN OPTologic (Grant No 899794); National Science Centre, Poland (Symfonia Grant No.2016/20/W/ST4/00314);

European Union’s Horizon 2020 research and innovation programme under the Marie-Sklodowska-Curie grant agreement No 101029393 (STREDCH) and No 847648 (“La Caixa” Junior Leaders fellowships ID100010434: LCF/BQ/PI19/11690013, LCF/BQ/PI20/11760031, LCF/BQ/PR20/11770012, LCF/BQ/PR21/11840013). PK acknowledges support from the Research Training Group “Differential Equation- and Data-driven Models in Life Sciences and Fluid Dynamics: An Interdisciplinary Research Training Group (DAEDALUS)” (GRK 2433) funded by the German Research Foundation (DFG).

---

\* paolo.stornati@icfo.eu

- [1] D. Banerjee and S. Chandrasekharan, Finite size effects in the presence of a chemical potential: A study in the classical nonlinear  $o(2)$  sigma model, *Physical Review D* **81**, 10.1103/physrevd.81.125007 (2010).
- [2] G. Aarts and F. A. James, On the convergence of complex langevin dynamics: the three-dimensional XY model at finite chemical potential, *Journal of High Energy Physics* **2010**, 10.1007/jhep08(2010)020 (2010).
- [3] S. Katz, F. Niedermayer, D. Negradi, and C. Torok, Comparison of algorithms for solving the sign problem in the  $O(3)$  model in 1+1 dimensions at finite chemical potential, *Phys. Rev. D* **95**, 054506 (2017), arXiv:1611.03987 [hep-lat].
- [4] J. Bloch, R. G. Jha, R. Lohmayer, and M. Meister, Tensor renormalization group study of the three-dimensional  $o(2)$  model, *Physical Review D* **104**, 10.1103/physrevd.104.094517 (2021).
- [5] S. Gupta, QCD at finite density, PoS **LATTICE2010**, 007 (2010), arXiv:1101.0109 [hep-lat].
- [6] V. Ayyar, S. Chandrasekharan, and J. Rantaharju, Benchmark results in the 2D lattice Thirring model with a chemical potential, *Phys. Rev. D* **97**, 054501 (2018), arXiv:1711.07898 [hep-lat].
- [7] M. C. Bañuls, K. Cichy, J. I. Cirac, K. Jansen, and S. Kühn, Density Induced Phase Transitions in the Schwinger Model: A Study with Matrix Product States, *Phys. Rev. Lett.* **118**, 071601 (2017), arXiv:1611.00705 [hep-lat].
- [8] H. Nielsen and P. Olesen, Vortex-line models for dual strings, *Nuclear Physics B* **61**, 45 (1973).
- [9] T. Banks, R. Myerson, and J. Kogut, Phase transitions in abelian lattice gauge theories, *Nuclear Physics B* **129**, 493 (1977).
- [10] A. M. Polyakov, Quark Confinement and Topology of Gauge Groups, *Nucl. Phys. B* **120**, 429 (1977).
- [11] G. ’t Hooft, On the Phase Transition Towards Permanent Quark Confinement, *Nucl. Phys. B* **138**, 1 (1978).
- [12] H. D. Trottier and R. M. Woloshyn, Flux tubes in three-dimensional lattice gauge theories, *Physical Review D* **48**, 2290 (1993).
- [13] M. Zach, M. Faber, and P. Skala, Flux tubes and their interaction in  $U(1)$  lattice gauge theory, *Nucl. Phys. B* **529**, 505 (1998), arXiv:hep-lat/9709017.
- [14] Y. Koma, M. Koma, and P. Majumdar, Static poten-

- tial, force, and flux-tube profile in 4D compact  $U(1)$  lattice gauge theory with the multi-level algorithm, Nuclear Physics B **692**, 209 (2004).
- [15] S. Chandrasekharan and U. J. Wiese, Quantum link models: A Discrete approach to gauge theories, Nucl. Phys. B **492**, 455 (1997), arXiv:hep-lat/9609042.
- [16] D. Banerjee, F.-J. Jiang, P. Widmer, and U.-J. Wiese, The  $(2 + 1)$ -d  $u(1)$  quantum link model masquerading as deconfined criticality, J. Stat. Mech. Theory Exp. **2013**, P12010 (2013).
- [17] D. Banerjee and A. Sen, Quantum scars from zero modes in an abelian lattice gauge theory on ladders, Phys. Rev. Lett. **126**, 220601 (2021).
- [18] N. Shannon, G. Misguich, and K. Penc, Cyclic exchange, isolated states, and spinon deconfinement in an  $xxz$  heisenberg model on the checkerboard lattice, Phys. Rev. B **69**, 220403 (2004).
- [19] O. Benton, O. Sikora, and N. Shannon, Seeing the light: Experimental signatures of emergent electromagnetism in a quantum spin ice, Physical Review B **86**, 10.1103/physrevb.86.075154 (2012).
- [20] D. Banerjee, Recent progress on cluster and meron algorithms for strongly correlated systems, Indian Journal of Physics **95**, 1669 (2021).
- [21] U. Schollwöck, The density-matrix renormalization group in the age of matrix product states, Annals of physics **326**, 96 (2011).
- [22] A. Celi, B. Vermersch, O. Viyuela, H. Pichler, M. D. Lukin, and P. Zoller, Emerging two-dimensional gauge theories in rydberg configurable arrays, Phys. Rev. X **10**, 021057 (2020).
- [23] D. Paulson, L. Dellantonio, J. F. Haase, A. Celi, A. Kan, A. Jena, C. Kokail, R. van Bijnen, K. Jansen, P. Zoller, and C. A. Muschik, Simulating 2d effects in lattice gauge theories on a quantum computer, PRX Quantum **2**, 030334 (2021).
- [24] E. Huffman, M. G. Vera, and D. Banerjee, Real-time dynamics of plaquette models using nisq hardware (2021).
- [25] M. Luscher, Volume Dependence of the Energy Spectrum in Massive Quantum Field Theories. I. Stable Particle States, Commun. Math. Phys. **104**, 177 (1986).
- [26] A. Honecker, J. Schulenburg, and J. Richter, Magnetization plateaus in frustrated antiferromagnetic quantum spin models, Journal of Physics: Condensed Matter **16**, S749 (2004).
- [27] M. Sarkar, M. Pal, A. Sen, and K. Sengupta, Quantum order-by-disorder induced phase transition in rydberg ladders with staggered detuning, arXiv preprint arXiv:2204.12515 (2022).
- [28] M. Aidelsburger, L. Barbiero, A. Bermudez, T. Chanda, A. Dauphin, D. González-Cuadra, P. R. Grzybowski, S. Hands, F. Jendrzejewski, J. Jünemann, G. Juzeliūnas, V. Kasper, A. Piga, S.-J. Ran, M. Rizzi, G. Sierra, L. Tagliacozzo, E. Tirrito, T. V. Zache, J. Zakrzewski, E. Zohar, and M. Lewenstein, Cold atoms meet lattice gauge theory, Philos. Trans. R. Soc. A **380**, 20210064 (2022).
- [29] E. A. Martinez *et al.*, Real-time dynamics of lattice gauge theories with a few-qubit quantum computer, Nature **534**, 516 (2016), arXiv:1605.04570 [quant-ph].
- [30] H. Bernien, S. Schwartz, A. Keesling, H. Levine, A. Omran, H. Pichler, S. Choi, A. S. Zibrov, M. Endres, M. Greiner, and et al., Probing many-body dynamics on a 51-atom quantum simulator, Nature **551**, 579–584 (2017).
- [31] C. Schweizer, F. Grusdt, M. Berngruber, L. Barbiero, E. Demler, N. Goldman, I. Bloch, and M. Aidelsburger, Floquet approach to  $\mathbb{Z}_2$  lattice gauge theories with ultracold atoms in optical lattices, Nature Physics **15**, 1168–1173 (2019).
- [32] A. Mil, T. V. Zache, A. Hegde, A. Xia, R. P. Bhatt, M. K. Oberthaler, P. Hauke, J. Berges, and F. Jendrzejewski, A scalable realization of local  $U(1)$  gauge invariance in cold atomic mixtures, Science **367**, 1128 (2020), arXiv:1909.07641 [cond-mat.quant-gas].
- [33] B. Yang, H. Sun, R. Ott, H.-Y. Wang, T. V. Zache, J. C. Halimeh, Z.-S. Yuan, P. Hauke, and J.-W. Pan, Observation of gauge invariance in a 71-site Bose–Hubbard quantum simulator, Nature **587**, 392 (2020), arXiv:2003.08945 [cond-mat.quant-gas].
- [34] M. Fishman, S. R. White, and E. M. Stoudenmire, The ITensor software library for tensor network calculations (2020), arXiv:2007.14822.

## Supplementary Material

*Numerical Implementation.*— For an efficient representation of the ground states in the quantum link ladder, we use matrix product states implemented in the `itensor` software package [34]. All the result presented in this work have been extrapolated to infinite bond dimension. During the numerical simulations, the bond dimension  $D$  of the matrix product state has been increased up to 1000 ( $D_{\max}$ ). We have also checked that the final state can be compressed with  $D < D_{\max}$ . The stopping criteria used in the optimization procedure is that the difference of the energy after 5 sweeps should be smaller than  $10^{-10}$ . For the larger volumes and close to the saturation, in the regime of the  $\mu_x \sim 1.8$ , the numerical simulation becomes unstable. If we run the optimization procedure different times, we might find different the ground state in different topological sectors. This phenomenon is caused because the energy gap between the different topological sectors approaches zero in the thermodynamic limit and close to the saturation regime. Since the gap in this region is smaller than the numerical precision, we could have found inconsistent result for certain parameter values. Nevertheless, we are still able to capture the important properties and extract physical information.

*Observables at  $\mu_x = \mu_y = 0$ .*— In this section, we briefly sketch the physics of the model at zero chemical potential, but for varying  $\lambda$  for completeness. This has already been discussed at length in [16] for periodic boundary conditions and using an efficient quantum Monte Carlo algorithm. It was demonstrated in that study that for large negative values of  $\lambda$ , where the  $J$  term is insignificant, the ground state physics is dominated by the states with the largest number of flippable plaquettes. This state spontaneously breaks both the charge conjugation and the lattice translation symmetry. For decreasing  $\lambda$ , however, the symmetry breaking pattern changes as the  $J$  term increases in strength. We encounter a phase where the charge conjugation symmetry is restored by the lattice translation symmetry remains broken. The two phases are connected by a weak first order phase transition.

For the quantum link ladder with  $L_y = 2$  and open boundary conditions in the  $x$ -direction, the symmetries are different. In particular, the lattice translation symmetry is not exact any more, while the charge conjugation symmetry is still exact. Thus, we expect a phase transition from a phase which breaks charge conjugation symmetry into a phase where the symmetry is restored. The susceptibility is expected to be large in the symmetry broken phase and vanish in the phase where the symmetry is restored. Figure 6 shows the expected behaviour of the susceptibility as a function of  $\lambda$  for three different lattice sizes.

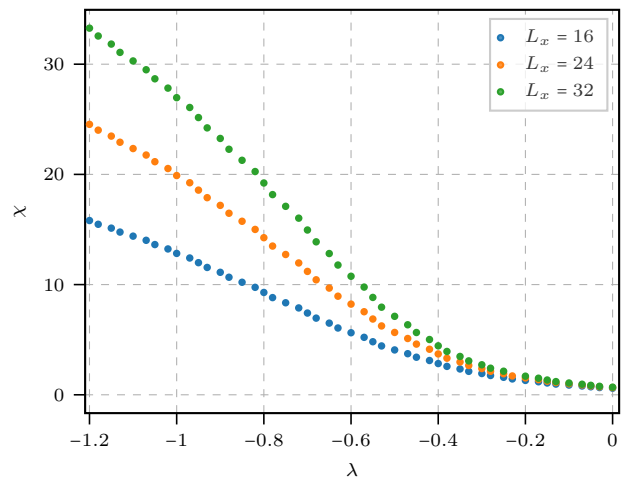


**FIG. 6:** Susceptibility as a function of  $\lambda$  at  $\mu_x = 0$ . The phase for large negative lambda has a broken symmetry, indicated by the increase in  $\chi$  with  $L_x$ . In the symmetry restored phase,  $\chi$  does not increase with the system size as expected.

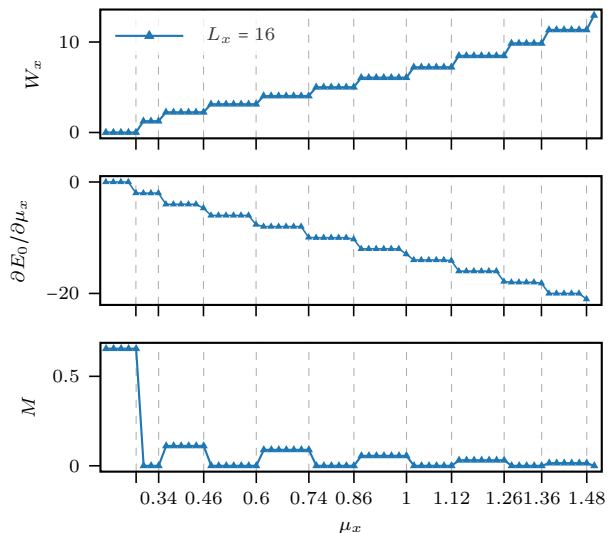


**FIG. 7:** (Top) Winding number sectors for  $L_x = 16$ . (Middle) The derivative of the ground state energy with respect to the chemical potential. (Bottom) The magnetization,  $M$ , defined as the difference of the plaquettes flippable in the clockwise and anti-clockwise fashion respectively.

*Observables at  $\mu_x > 0$ .*— As the  $\mu_x$  is cranked up (keeping  $\mu_y = 0$ ), we study the behaviour of the expectation of the winding number  $\langle W_x \rangle$ , and the derivative of the ground state energy  $E_0$  with respect to  $\mu_x$ ,  $\frac{\partial E_0}{\partial \mu_x}$ . In the top and the middle panel in Figure 7, we plot the two quantities. As expected from the Feynman-Hellman theorem, these two quantities show the same qualitative behaviour upto a constant factor (with an overall negative sign). Finally, we also plot the flippability of the plaquettes,  $M$ . The flippability is defined as the difference between the total number of plaquettes which are flippable in the clockwise fashion and the ones which are

flippable in the anti-clockwise fashion. Interestingly, this observable shows a staggered behaviour between zero and

non-zero values for odd and even winding number of electric fluxes respectively. This is a clear indication of a cooperative behaviour of the plaquettes across the lattice.